# High Resolution Portable Platform for pH sensing via Colorimetric Fluorescence of Carbon Dots

Gianluca Minervini[a,b,c], Annamaria Panniello[c], Daniel Quesada-González[a], Gabriel Maroli[a,e], Elisabetta Fanizza[c,d], Marinella Striccoli[c], Ruslan Álvarez-Diduk[a]*, Maria Lucia Curri[c,d]*, Arben Merkoçi[a,f]*

[a] Catalan Institute of Nanoscience and Nanotechnology (ICN2), CSIC and BIST, Campus UAB, Bellaterra, 08193 Barcelona, Spain

[b] Department of Electrical and Information Engineering, Polytechnic of Bari, via Orabona 4, 70126 Bari, Italy

[c] CNR-Institute for Physical and Chemical Processes (IPCF), via Orabona 4, 70126 Bari, Italy

[d] Chemistry Department, University of Bari "Aldo Moro", via Orabona 4, 70126 Bari, Italy

[e] Research Institute of Electrical Engineering (IIIE) "Alfredo Desages", National University of the South, CONICET- Argentina.

[f] Catalan Institution for Research and Advanced Studies (ICREA); Passeig de Lluís Companys, 23, Barcelona, 08010, Spain

***** Corresponding Authors: Ruslan Álvarez-Diduk: ruslan.alvarez@icn2.cat; Maria Lucia Curri: marialucia.curri@uniba.it; Arben Merkoçi: arben.merkoci@icn2.cat.

## Abstract

Portable sensing platforms based on nanoparticles are becoming increasingly significant across diverse fields, as they enable real-time measurements in various environments without complex lab protocols. Carbon dots (CDs), known for low toxicity and intense fluorescence, can exhibit pH-dependent optical emission, generally related to proton exchange-capable surface groups. In addition, CDs' hydrophilicity, biocompatibility, and stability make them advantageous for pH sensing and, despite limited application in portable sensing devices, their full potential can be realized with precise control of chemistry and optical properties. In this study, we fabricate a

portable nitrocellulose-based platform for pH sensing, expressly designed to take advantage of the fluorescence properties of resorcinol-based CDs. First, responsivity of CDs fluorescence features on pH is carefully spectroscopically characterized and linked to acid-base equilibria of polyphenols (hydroxylated polyaromatic rings) present within the CDs carbonaceous structure. Notably, this also offers a titrimetric method to estimate CD concentration. Next, nitrocellulose-based wax-printed circular pads are functionalized with CDs and integrated with a smartphone-based fluorescence colorimetric optical detection system. The developed portable device exhibits a measurement resolution of ±0.2 pH units (in the range between 2.5 to 6.7) and of ±0.3 pH units (in the 6.7 – 7.0 range), compatible with most practical pH measurement needs in biological, food and drink, wastewater sample analysis and others. Moreover, although some portable pH sensing devices are already widespread and commercially available, this platform is easy to use, it necessitates only very small sample volumes and is potentially adaptable to various environments and automated analysis processes that does not need prior-use calibrations.

***Keywords.*** carbon dots, fluorescence, pH, paper sensor, smartphone detection, colorimetry.

## 1. Introduction

In current real-world applications pH sensing is typically conducted using three-electrode potentiometry (pH meters) or colorimetric pH test paper strips [1–4]. Specifically, potentiometric pH meters offer a broad detectable pH range and very high resolution, while pH test strips provide rapid pH testing, compatible with user-friendly procedures. However, in some practical scenarios, these methods still suffer from limitations hindering their complete suitability. For instance, using pH meters implies dealing with some drawbacks such as electrode vulnerability, the need for large

sample volumes, necessity of frequent calibration and trained operators. On the other hand, in most usual cases, commercial pH test strips are characterized by measurement resolutions not higher than ca. ±0.5 pH units [5,6]. Furthermore, certain colorimetric tests require visual interpretation of the results, which can be disadvantageous due to the potential for personal color biases in determining pH values [7,8].

In response to these colorimetric detection limitations, recent efforts have aimed at advancing such classical pH testing methods. This has led to the fabrication of sophisticated pH sensor devices with optical detection, as emphasized by several works reported in the scientific literature [8–22] and in recently patented inventions [23–25]. Generally, these advanced devices consist of an active pH sensing material embedded or deposited onto a substrate matrix (often paper- or polymer-based). The active material responds to pH variations with detectable alterations of its optical properties. In particular, the revelation of such optical property variations, either via smartphone- or desktop-scanner-based detection then enables improvements on measurement objectivity and accuracy [8,12,14–16,18–22]. Nevertheless, such innovative pH sensing platforms often face technical limitations, including a narrow dynamic range (sometimes limited to few pH units), long response times, the need for large sample volumes , and accuracy in pH determination not significantly higher than that of commercial pH strips [9–11,13,16,17,19–22]. Moreover, other reported methods require multi-step fabrication procedures (e.g. based on high-resolution laser patterning of the substrate, or ink-jet printing using separate custom-made inks) that must be devised with extensive care to ensure the proper working of the final sensing device [8,12–15,17–22]. Thus, there is generally still demand for development of robust and high-performing colorimetric pH sensors.

CDs, zero-dimensional carbonaceous nanoparticles characterized by visible-light

fluorescence, have attracted attention as pH sensing materials since early stages of their discovery [26–28]. These nanoparticles typically have a size between 1 and 10 nm and they are chemically composed of non-toxic light elements (C, O, H, and eventually N, S, P, B, …) [29–33]. Many CDs synthesized via carbonization of water-soluble molecules naturally exhibit fluorescence properties that respond to pH changes [27,28]. This responsiveness is typically ascribed to the presence of acid/base active surface chemical groups, such as –COOH, –$NH_2$, –OH, etc. [26]. Therefore, CDs have been widely reported as pH-sensitive materials in aqueous dispersions [26–28]. More specifically, depending on their spectroscopic features, single-band emitting CDs have been employed for pH sensing based on fluorescence quenching, while multiple band emitting CDs have been often proposed for ratiometric fluorescence sensing [34–38].

Often, CDs are used directly in solution-based analyses, providing highly accurate pH measurements [26,39,40]. Nevertheless, these techniques necessitate benchtop instrumentation and experienced personnel. Meanwhile, the incorporation of these nanoparticles into portable platforms has been reported in few examples. Wang et al. [41] prepared pH test strips embedding orange-emitting CDs that exhibited naked-eye observable changes in fluorescence intensity across the pH range of 1–14 when examined under UV light. Zhang et al. [42] ink-jet printed pieces of filter paper with tricolor emitting CDs to obtain pH test strips that could successfully measure pH in a broad range by visual inspection of color changes. Huo et al. [43], reported a polymer based pH sensor based on CDs as sensing materials that, after soaking for 5 s in a buffer solution, allowed quantitative pH assessment after recording the fluorescence with a spectrofluorometer and employing fluorescence or colorimetry to quantify the sensing signal. Thus, in spite of the large number of papers reporting pH sensing with CDs in solution, the application of these nanoparticles in portable platforms using advanced optical signal registration remains limited and needs to be

further explored.

With this motivation, in this work, we develop a portable pH sensing platform based on colorimetric fluorescence CD detection. Dual emissive CDs are synthesized by polycondensation of resorcinol and containing acid-base optically responsive hydroxylated polyaromatic rings [44]. The mechanism enabling the pH sensing relies entirely on the fluorescence properties of the CDs. First, the fluorescence pH responsivity of the CDs is carefully examined and correlated to acid-base equilibria at the molecular level. Then, the fluorescent nanoparticles are used to functionalize wax-printed pads on a nitrocellulose substrate. Fluorescence changes with pH are assessed using colorimetric image analysis, which allows achieving high-resolution pH measurement, reaching ±0.2 pH units in the range from 2.5 – 6.7 pH range and ±0.3 pH units in the 6.7 – 7.0 range. Overall, the approach presented herein is compatible with a broad variety of samples and working conditions and hence can have applicative relevance for pH sensing in several areas.

## 2. Materials and Methods

### 2.1 Chemicals

Resorcinol (≥99%, Sigma Aldrich), ethylene glycol (EG, ≥ 99%, Sigma Aldrich), sodium hydroxide (NaOH, ≥97%, Sigma Aldrich), hydrochloric acid (HCl, 37%, Sigma Aldrich), disodium hydrogen phosphate ($Na_2HPO_4$, 98-100.5%, Sigma Aldrich), monosodium dihydrogen phosphate ($NaH_2PO_4$, ≥99.0%, Sigma Aldrich), citric acid (99%, Sigma Aldrich), L-ascorbic acid (AA, 99%, Sigma Aldrich), sodium carbonate ($Na_2CO_3$, ≥99.5%, Sigma Aldrich), sodium bicarbonate ($NaHCO_3$, ≥99.7%, Sigma Aldrich). McIlvaine (citrate-phosphate) buffer solutions at pH ranging from 8 to 2.2 were obtained mixing stock solutions of 0.1 M citric acid and 0.2 M $Na_2PO_4$ in different volume ratios up to reaching a final volume of 5 mL.[45] Carbonate-

Bicarbonate buffer at pH 10 was analogously obtained by mixing adequate volumes of 0.1 M stock solutions of $Na_2CO_3$ and $NaHCO_3$. All aqueous solutions were prepared using MilliQ water.

## 2.2 Preparation of CDs

CDs were synthesized following a procedure previously reported in [44]. In details, a solution of resorcinol (1.5 g) in EG (3 mL) was added to 12 mL of EG previously heated in a round bottom flask that was kept open through all the duration of the reaction. Soon after resorcinol solution injection, 500 μL of a 2 M NaOH aqueous solution were quickly added, serving as a catalyst for resorcinol carbonization. The reaction temperature in the round bottom flask was monitored and kept constant *via* a temperature controller connected to a heating mantle by a thermocouple placed inside the flask. After synthesis, the obtained CDs were purified by a series of four successive centrifugation steps, using a very diluted (~$10^{-4}$ M) HCl aqueous solution to recollect and precipitate the nanoparticles. More specifically, after each centrifugation step at 9000 rpm for 30 min, the supernatant was removed and discarded, while the purified precipitate was redispersed adding ~$10^{-4}$ M HCl solution. Finally, after four centrifugation cycles, the dark precipitate was dried under vacuum. The as-obtained purified CDs were finally dispersed in aqueous buffer solutions for further uses.

## 2.3 Spectroscopic analysis of CD optical properties

UV-Vis absorption spectra were acquired with a Cary 5000 spectrophotometer (Agilent Technologies, Inc., Santa Clara, CA, USA). Photoluminescence (PL) spectra were measured with a Fluorolog 3 spectrofluorometer (HORIBA Jobin-Yvon GmbH, Bensheim, Germany) equipped with a 450 W Xe lamp as the excitation source and with double-grating excitation and emission monochromators. All measurements were performed on dispersions of CDs in aqueous buffer solutions, in a quartz cuvette (Hellma Analytics, Milan, Italy) with a 1 cm optical path. To avoid

photon re-absorption in these measurements, all solutions were diluted so that the absorbance registered at the maximum of the lower energy absorption band was less than 0.1.

## 2.4 pH-sensitivity of CDs experiments in solution

Purified CD powders were dispersed in a phosphate buffer solution (0.1 M, pH = 7) that was previously prepared by mixing suitable concentrations of $Na_2HPO_4$ and $NaH_2PO_4$. Subsequently, 1 mL of such CD dispersion (having a concentration of 5 μg/mL) was subjected to the incremental addition of a 1 M HCl aqueous solution ($HCl_{aq}$). Specifically, at each step of HCl addition, 5 μL of $HCl_{aq}$ were added and UV-Vis absorption and PL ($\lambda_{exc}$ = 350 nm, $\lambda_{exc}$ = 485 nm) spectra were recorded. The experimental procedure was concluded upon reaching a total added volume of 105 μL, as no further discernible spectroscopic changes were observed. To account for the dilution introduced upon addition of the $HCl_{aq}$, the as-recorded spectra were multiplied by a factor:

$$D=\frac{V_{in}+V_{add}}{V_{in}} \quad (1)$$

where $V_{in}$ is the initial volume of the CD dispersion and $V_{add}$ is the added volume of HCl.

## 2.5 Fabrication of CD-based nitrocellulose pads and smartphone-based fluorescence detection

A nitrocellulose membrane strip (Unisart® CN95, Sartorius) was patterned to create circular nitrocellulose pads (CNPs) with a diameter of 2.5 mm spaced by a 1.5 mm distance. The pattern was created by printing a black hydrophobic wax using a Xerox ColorQube 8580 solid ink printer. After printing, the nitrocellulose strip was kept on a hot plate at 90 °C for 30 s to allow diffusion of the hydrophobic wax across the entire thickness of the nitrocellulose, thus creating a complete lateral confinement of the circular pad.

Then, the CNPs were functionalized by drop-casting 2 μL of a pristine aqueous dispersion of CDs, followed by drying on a hot plate at 50 °C for 15-20 min, until complete water evaporation. Thus, functionalized circular nitrocellulose pads (F-CNPs) were obtained. To construct the calibration curves, the F-CNPs were drop-casted with 2 μL of McIlvaine buffer solutions at different pH values.

The resulting modifications of CD fluorescence were then analyzed with a Microscopy Cube Assembly (TLV-U-MF2, THORLABS©), equipped with an excitation filter (MF390-18, 390 ± 9 nm), a dichroic filter (MD416 425 – 575 nm) and optional emission filters (MF460-60, 460 ± 30 nm, referred to as "blue emission filter" or MF530-43, 530 ± 20 nm, referred to as "green emission filter"). The employed setup allowed irradiating and analyzing four F-CNPs in each single acquisition. Each pool of four pads contained one pad drop-casted with a pH 8 McIlvaine buffer, that was used as internal reference in the case of single-channel intensity analyses.

The fluorescence was then detected recording digital pictures with a smartphone camera (Realme GT NEO 3T) in manual mode, autofocus, ISO at 100 and adjusting the shutter speed in order to optimize the exposure conditions.

## 3. Results and discussion

### 3.1 CDs preparation, characterization and PL mechanisms underlying pH responsivity

The preparation of CDs employed for the portable platform relies on a method reported in [44] and is schematized in Fig. 1a. The synthetic approach involves thermal polycondensation of

resorcinol in ethylene glycol solvent and basic-catalyzed environment. This leads to the formation of CDs containing PPs, i.e. hydroxylated polyaromatic molecules, deriving from resorcinol polycondensations.

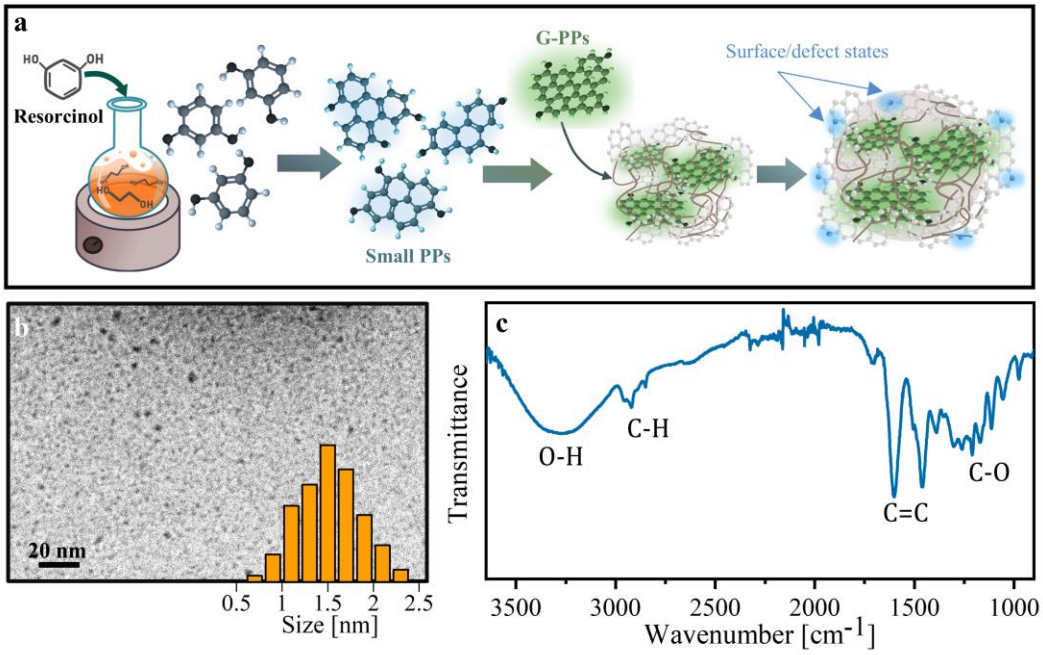


**Fig. 1.** (a) Scheme of synthetic preparation of CDs and of formation of fluorescent PPs in the nanoparticles during the reaction. (b) TEM micrograph and size distribution histogram (inset) and (c) FT-IR spectrum of the CDs.

The CDs are observable in TEM micrographs as spheroidal dots having a mean size of $1.5 \pm 0.3$ nm (Fig. 2b). The FT-IR spectrum of CDs displays a broad band ascribed to O–H stretching (at 3320 – 3600 $cm^{-1}$), some weak peaks in the 2800 – 3000 $cm^{-1}$ interval due to C–H stretching, some signals due to C=C stretching (at 1650 – 1750 $cm^{-1}$) and peaks in the region 1000 – 1300 $cm^{-1}$ due to C–O stretching. Such FT-IR analysis highlights that the CD surface contains hydroxyl groups. Moreover, both aromatic and aliphatic carbon structures are identified in the CDs. Additionally, the broad O–H stretching band indicates the formation of hydrogen

bonds between the alcohol functionalities. This aligns well with model in [44]. that describes CDs as consisting of PPs incorporated in a carbogenic nanoparticle matrix, interconnected by EG-aliphatic structures and stabilized via hydrogen bonds.

The sensing mechanism in the portable platform derives from the response of the CD, particularly to the response of this fluorescence to pH, and needs to be further assessed. UV-Vis absorption and (PL) spectra of resorcinol-derived CDs are reported in Fig. S1. The CD absorption spectrum exhibits a narrow band at around 500 nm and an extended absorption at $\lambda < 400$ nm. The emission spectrum consists of a blue and a green PL band. As recently demonstrated in [44] and resumed in Table S1 these are respectively ascribed to emission by surface or defect states and to the molecular emission of green emitting PPs (G-PPs).

To specifically test in detail the reversible responsivity of CD fluorescence to pH changes, we carried out an experiment in which CDs in solution were progressively added with a very small number of HCl moles, while modifications of spectroscopic absorption and emission features were monitored after each addition. For this experiment, first, CDs were dispersed in a phosphate buffer at pH 7 and then mixed with 5 μL of 1 M solutions of HCl in successive steps (see Sec. 2.4 for further details). Spectroscopic changes observed in UV-Vis absorption and PL spectra ($\lambda_{exc}$ = 485 nm) after each HCl addition are reported in Fig. 2a-b.

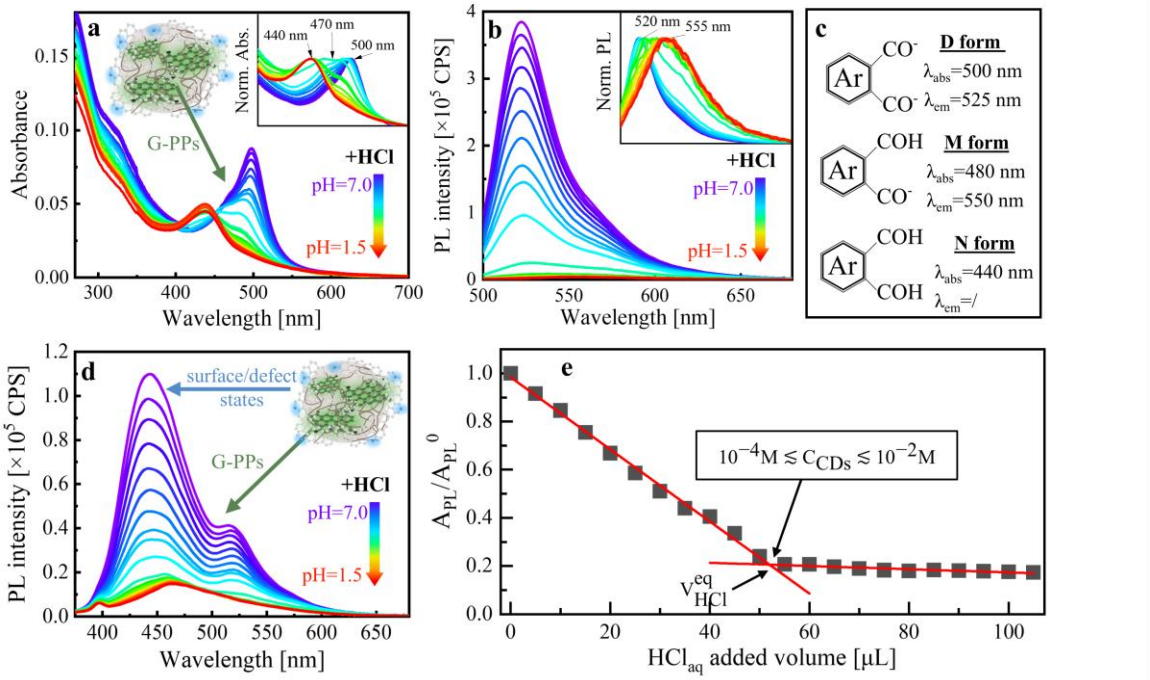


**Fig. 2.** (a) UV-Vis absorption and (b) PL ($\lambda_{exc}$ = 485 nm) spectra of a CD dispersion at increasing HCl concentration, with top-right insets showing normalized spectra and peak positions; (c) scheme of the dianion (D), monoanion (M) and neutral (N) forms of the green-emitting polyphenols (G-PPs), including their absorption and emission peak positions; (d) PL spectra ($\lambda_{exc}$ = 350 nm) of CDs at increasing HCl concentration. Insets of (a) and (d): scheme of the CDs designating with blue and green band assignments, initial and final pH; (e) fluorescence titration curve reporting the ratio between PL spectrum areas $\lambda_{exc}$ = 350 nm ($A_{PL}$) and that of the pristine solution spectrum ($A_{PL}^0$) as a function of the volume of added titrant.

Upon the incremental HCl addition, the absorption band at 500 nm of the pristine CDs dispersion exhibits a gradual dampening and a large blue shift (Fig. 2a). Specifically, Fig. 2a inset clearly shows that the pristine absorption band undergoes a transition to a band at 470 nm and

finally to a band peaked at 440 nm. In parallel, a substantial quenching of the green PL peak (Fig. 2b), with a progressive red shift of the pristine band (Fig. 2b inset), is noted.

Such spectroscopic variations can be explained considering the possible proton-exchanging equilibria of PPs in dependence of pH. In fact, it is known that hydroxylated polyaromatic molecules can have pKa in physiological pH ranges [46–48] and that the surface of these CDs is negatively charged due to the hydroxyl groups' deprotonation [44]. Therefore, to rationalize the observed spectroscopic changes with HCl addition, we can safely consider that in the pristine solution (at pH 7) the G-PPs have some $–CO^-$ groups that can quantitatively react with $H^+$. Upon HCl addition, these groups are progressively protonated to –COH, leading to the observed spectroscopic modifications. Conversely, after reaching a pH of 1.5, the absence of additional changes upon further HCl addition suggests that, under these pH conditions, the polyaromatic fluorophores lack $–CO^-$ groups that can quantitatively react with $H^+$. Thus, the spectral band shifts and modifications observed both in absorption and PL can be collectively explained considering three distinct acid/base conjugated forms for the G-PPs (Fig. 2c), namely: (i) a dianion (D) form responsible for the pristine absorption at 500 nm and emission at 520 nm, (ii) a monoanion (M) form absorbing at around 470 nm and weakly emitting at 555 nm and (iii) a neutral (N) form, that has the absorption band peaked at 440 nm and no emission within the investigated spectral range.

To demonstrate the reversibility of the acid-base reactions between the D, M and N forms, the acidified dispersion of CDs (pH 1.5) was progressively added with 5 μL of a 1 M NaOH aqueous solution. The resulting spectroscopic data collected after each NaOH addition are reported in Fig. S2a-b. It can be observed that NaOH addition leads to a fluorescence restoration retracing the spectroscopic changes of the HCl quenching. However, a slight loss of fluorescence intensity

is observed, as demonstrated by the difference between the restored PL intensity at pH 7 and the original one, that is ascribed to irreversible phenomena occurring during such experiments, such as nanoparticle aggregation or irreversible chemical modifications of the emitting units within the CDs, hindering the complete reestablishment of the original fluorescence intensity [44].

The overall PL spectrum consists of a blue and a green PL band, as can be revealed exciting the CDs in the UV range (Fig. S1). Thus, to provide a comprehensive overview of pH sensitivity of both CD emission bands, we examined the variations in the PL spectra obtained after HCl and NaOH additions exciting at 350 nm (Fig. 2d, Fig. S2c).

With the progressive increase of added HCl, both blue and green PL bands exhibit a gradual decrease in the intensity. On the other hand, addition of NaOH to the quenched solution leads to restoring both bands, with a fluorescence loss (Fig. S2c). Remarkably, upon quenching and restoration, the relative intensities of the blue and green PL bands undergo variations. This can be easily shown for instance, by plotting the ratio of the intensities of the two bands recorded at their maxima (i.e. 445 nm and 520 nm), as a function of volume of added titrants (namely HCl and NaOH), as shown in Fig. S3. For the quenching experiment, the ratio between blue and green PL band intensities shows two uniform progressive decrease trends in the range of added titrant (i.e. HCl) volume from 0 to 45 μL and from 60 to 105 μL, interspaced by a small increasing trend from 45 to 60 μL. On the other hand, in the restoration experiment the ratio undergoes an increase upon addition of the first 10 μL of titrant (i.e. NaOH), then it remains constant up to a volume of 70 μL, after which it progressively increases up to reach around the value of the pristine solution at the added NaOH volume of 105 μL. The results collectively show that the individual blue and green PL bands not only can be reversibly quenched and restored, but also their ratio undergoes some reversible variations as an effect of quantitative reactions with HCl and NaOH. Notably, this

281 change of blue-to-green relative intensities constitutes the foundation for the application of the
282 fluorescence colorimetry approach, as described in the following.

283 From an applicative perspective, it is also noteworthy that, despite the high sensitivity of
284 the blue and green PL bands to pH, the PL of the nanoparticles remains unaffected by other
285 possible interferents, such as metal cations or biological vitamins, even at high concentrations
286 ($\geq$ 50 mM). The potential interference of these species in pH analysis was suitably evaluated, and
287 the results are provided in the SI (see Fig. S4 – S6).

288 Furthermore, the discovery that also the blue PL band alone exhibits a reversible pH
289 sensitivity, indicates that, akin the G-PPs, surface and/or defect groups responsible for this PL
290 band undergo reversible chemical protonation reactions. In particular, considering that the
291 chemical composition of CDs is characterized by variably protonated hydroxyl functionalities, [44]
292 it may be recognized that these groups are reversibly protonable $–CO^-$ groups.

293 Thus, considered collectively, the results of the previous experiments evidence that the titrant (HCl)
294 quantitatively reacts with both (i) G-PPs and (ii) $–CO^-$ groups of different PPs that can undergo
295 protonation reactions. This may also spontaneously inspire to consider the quenching experiment
296 (Fig. 2d) as a fluorometric titration of such species featuring reversibly protonable $–CO^-$ groups
297 (Fig. 2e). In particular, with appropriate considerations on the reaction stoichiometry and on the
298 density of emitting units present in each nanoparticle, we can correlate the volume of titrant at the
299 equivalence point ($V_{HCl}^{eq}$) to the molar concentration of nanoparticles in the dispersion ($C_{CDs}$), with
300 the equation:

301 $$C_{CDs} = \frac{C_{HCl} V_{HCl}^{eq}}{s_m d_{EM} V_{in}} \qquad (2)$$

where $C_{HCl}$ is the concentration of the titrant stock solution, $V_{in}$ is the initial volume of the pristine dispersion of CDs, $s_m$ is the average stoichiometry of reactions of $H^+$ and $d_{EM}$ is the density of emitting units per CD. Complete details regarding the derivation of Eq. (2) are provided in the SI.

It is interesting to note that Eq. (2) may allow estimating the concentration of CDs in a dispersion by means of a titration method, i.e. measuring the volume of titrant at the equivalence point. However, it is evident that a precise $C_{CDs}$ obtainment needs that $s_m$ and $d_{EM}$ are known. In turn, accurate assessment of these quantities demands additional expressly focused experimental procedures, and/or a very extensive theoretical modelling of the carbonaceous nanoparticles. Therefore, the correct calculation or experimental determination of $s_m$ and $d_{EM}$ is not the scope of this work. However, the orders of magnitudes of these quantities can be reasonably individuated. In the SI, a detailed discussion is provided in which the approximate orders of magnitude for the upper and lower bounds of $s_m$ and $d_{EM}$ are rationally examined. By setting such rough bounds for $s_m$ and $d_{EM}$ and substituting the measured $V_{HCl}^{eq}$ in Eq. (2), a reasonable range of order of magnitude for $C_{CDs}$ can be evaluated, which is between $10^{-4}$–$10^{-2}$ M. In general, it is worth remarking that a more precise estimation of $s_m$ and $d_{EM}$ would result in a better estimate of the CD concentration. This could represent a significant stride towards establishing reliable procedures for determining the amount of CDs in a solution, a critical advancement for broadening the practical applications of CDs across various fields.[49]

## 3.2 Design of nitrocellulose-based platform and its sensing mechanism

The nitrocellulose-based platform exploits the intriguing fluorescence response of CDs due to reversible protonation of G-PPs and hydroxyl surface groups. The preparation of the nitrocellulose substrate consisted in a simple fabrication of CNPs, by printing a hydrophobic wax

(the complete experimental procedure is described in the Experimental Section). After their preparation, the CNPs were functionalized by drop-casting an aqueous CD dispersion, followed by water evaporation under soft heating. CDs were thus immobilized on the surface of the CNPs yielding F-CNPs.

The principle underlying pH sensing in the platform can be summarized as follows: upon drop-casting a calibration solution (McIlvaine buffer, composed by a citrate-phosphate acqueous solution) onto the F-CNPs, a fraction of the CDs in the F-CNPs are solubilized in the aqueous phase of the deposited drop. Once in the aqueous phase, interaction of CDs with $H^+$ in the buffer solution leads to alterations of the CD fluorescence that are analyzed by a smartphone-based detection system. In particular, the optical revelation device is equipped with mirrors and filters suitable for discrimination of the blue and green fluorescence contributes deriving from the CDs (Fig. 3) (for further technical specifications see Experimental Section).

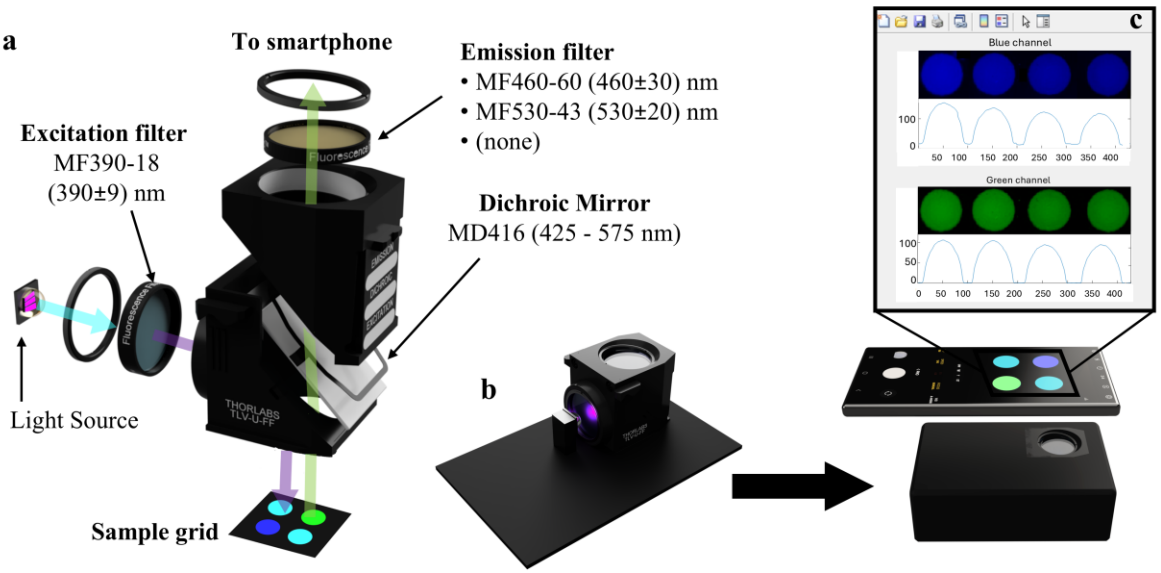


**Fig. 3.** (a) scheme of the fluorescence detection system equipped with dichroic mirror and optical excitation and emission filters. Optical emission filters with bandwidths of (460 ± 30) and (530 ± 20) nm are denoted in the text as "blue" and "green" emission filters respectively; (b)

overview of the portable fluorescence detection device operating with the smartphone; (c) software-based analysis of the fluorescence from CDs in the functionalized circular nitrocellulose pads (F-CNPs). More details on fluorescence digital picture analysis are reported in the following section regarding the calibration of nitrocellulose pad fluorescence for pH sensing.

## 3.3 Calibration of nitrocellulose pad fluorescence for pH sensing.

Within the pH sensing strategy of the developed platform, the fluorescence signal needs to be maximized adjusting the concentration and protonation state of the pristine CD dispersion employed to obtain the F-CNPs. First, the concentration of CDs deposited in the F-CNPs is a pivotal parameter to calibrate as it will influence the overall fluorescence intensity. CD concentration in the initial dispersion was calibrated by depositing pristine CD dispersions at increasing nanoparticle concentration on CNPs. The PL was then revealed using the smartphone-based apparatus (Fig. 3). Smartphone recorded digital pictures were acquired at different exposure times, obtained by modulating the shutter speed in the range 0.2 – 0.5 s and employing blue and green emission optical filters (Fig. 4). Following acquisition, the digital pictures were processed to separate their three-color channels: Red (R), Green (G) and Blue (B). Details of such image analysis procedure are described in the SI (see Fig. S7). Subsequently, as shown in Fig. 4c-d, the intensity of each channel is analyzed separately. Then, the fluorescence is evaluated quantitatively from the intensities of B or G channels, as shown in Fig. 4e-f.

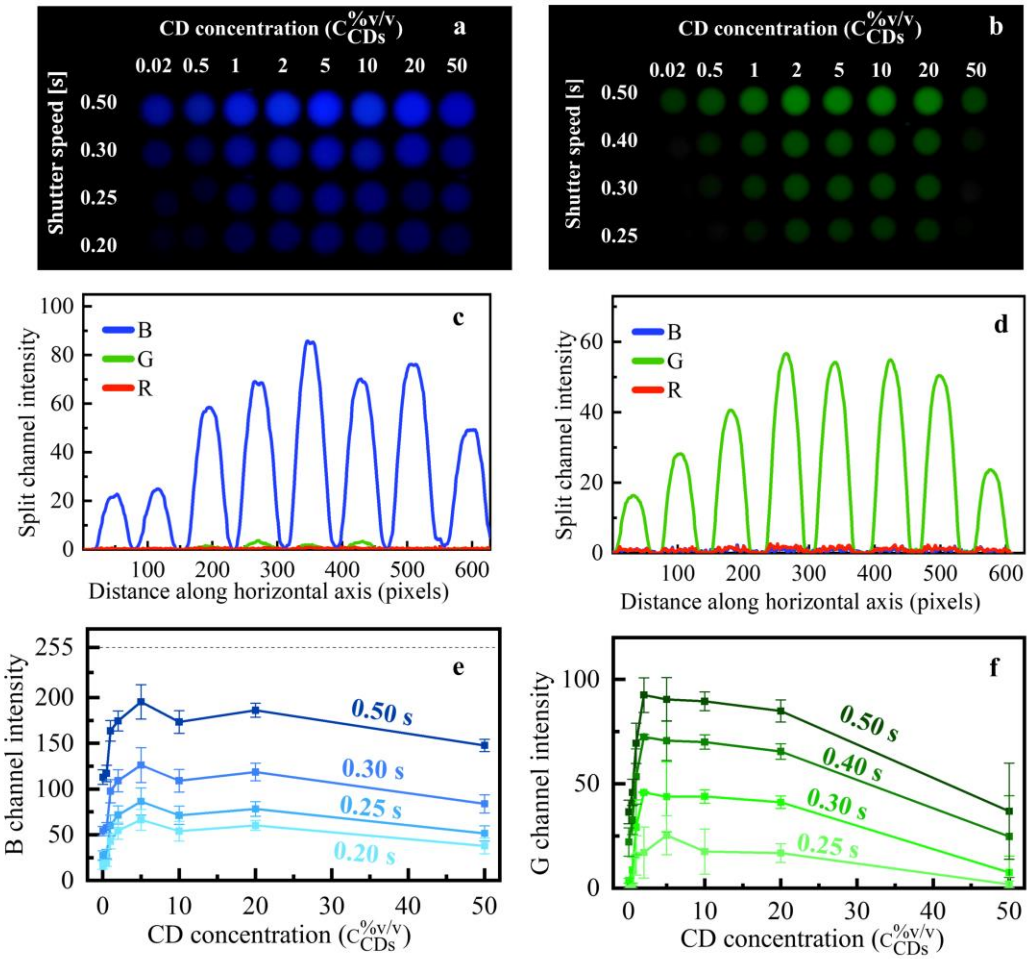


360

361 **Fig. 4.** (a), (b) smartphone recorded digital pictures of the F-CNPs at different shutter speeds and
362 CD concentrations ($C_{CDs}^{\%v/v}$); (c), (d) plots of B, G and R channels as a function of the distance along
363 the horizontal axis of the picture (F-CNPs spots at the third row of (a), (b) were selected as
364 representative, corresponding to shutter speed of 0.25 and 0.30 s for the B and G channels
365 respectively), and (e), (f) resulting B and G channel intensities of F-CNPs drop-cast with CD
366 dispersions at $C_{CDs}^{\%v/v}$ from 0.02 to 50%$_{v/v}$. Pictures and B, G channel intensities have been acquired
367 using (a), (c), (e) blue emission filter and shutter speed in the range of 0.20 – 0.50 s and (b), (d),
368 (f) green emission filter and shutter speed in the range of 0.25 – 0.50 s. The upper scale limit of

the grayscale range (0 – 255) is highlighted in (e) as a guide for the eye. The error bars are standard deviations calculated from three experiment replicates.

From Fig. 4c it appears evident that the use of the blue emission filter leads to a fluorescence signal exclusively in the B channel and only very low residual signal intensity is noted in the G channel, while the R channel registers only noise. Vice versa, upon the application of the green emission filter (Fig. 4d), only the G channel reveals a discernible signal, while the B and R channels exhibit noise exclusively. This confirms that the blue and green emission filters allow independent analysis of the spectroscopic blue and green PL bands of the CDs (Fig. 2b, Fig. 2d, Fig. S1).

The signal intensities of B and G channels obtained after quantitative digital image analysis (Fig. 4e-f) allow assessing the alterations of fluorescence intensity of blue and green PL bands due to changes in nanoparticle concentration and shutter speed. For both B and G channels, the intensity increases linearly with the CD concentration up to 2 %; then, a saturation range is observed in the 2 – 20 % interval, as the points of recorded intensities in this range are invariant within the experimental error. Subsequently, a decrease of fluorescence intensity is obtained upon further CD concentration increase beyond 20% up to 50 %.

Such fluorescence self-quenching phenomenon at increasing concentration occurs in numerous fluorophores, [50–52] including CDs [53–57] and it is often ascribed to the re-absorption of emitted photons due to overlapping of absorption and fluorescence bands, or to transfer processes. Remarkably, the results in Fig. 4e-f highlight that the dampening due to photon re-absorption is more pronounced for the G intensity than for B intensity. This tightly agrees with the spectroscopic properties of CDs (Fig. S1) and can be explained considering that the green

emission band has a very small Stokes shift. This remarks how changes in CD spectroscopic features observed in cuvette and using a benchtop spectrofluorometer (see Sec. 2.3) are retained in the B and G channels after deposition on CNPs and image analysis. It also worth to note that the trends of B and G channel intensity with $C_{CDs}^{\%v/v}$ result independent from the shutter speed, that just alters the intensity of the recorded PL but not the trend of the intensity with $C_{CDs}^{\%v/v}$. This points out that the exposure time can be flexibly adjusted within the interval from 0.2 to 0.5 s, to optimize the signal-to-noise ratio in the resulting pictures.

Besides nanoparticle concentration, the state of protonation of $–CO^-$ groups of CDs is another crucial parameter to optimize. In fact, protonation of hydroxyl groups determines alterations of the overall PL intensity emitted by the CDs (Fig. 2, Fig. S2), and also of the ratio between blue and green PL bands (Fig. S3). Within the preparative approach, the protonation state of CDs can be modified by altering the pH of the pristine dispersion employed for the functionalization of CNPs. Thus, we tested different combinations of $C_{CDs}^{\%v/v}$ and pH values of pristine CD dispersion, aimed at identifying the appropriate combination of parameters able to maximize the responsivity to pH.

The detailed procedure of simultaneous pH and $C_{CDs}^{\%v/v}$ optimization of the pristine CD dispersion is provided in the SI (Table S2-S3, Fig. S8 – S9). More specifically, we tested $C_{CDs}^{\%v/v}$ in the range of 5 – 20 %, based on the finding that this saturation range allows nanoparticle concentration adjusting without significant effects on fluorescence intensity (Fig. 4e-f). Furthermore, we tested pristine solution pH in the range of 7 – 10, based on the observation that the overall PL of the CDs is maximum at pH > 7, as indicated in Fig. S8a, where the samples at fixed $C_{CDs}^{\%v/v}$ show brighter spotlights at higher pH values. For each examined case of F-CNP, a calibration curve was constructed, thus allowing association of the parameters for CNP

functionalization with the sensing performance. These calibration curves were obtained by drop-casting F-CNPs with McIlvaine buffer solutions in the pH range between 2.2 and 7 (Fig. S8c). The procedure aimed at finding concentration and pH values of the CD pristine dispersion leading to the best balance between wide pH dynamic range, high resolution in pH measurements, high fluorescence intensity (leading to high signal-to-noise ratio in the acquired images) and low spurious background signals. On the other hand, picture acquisition parameters, such as the shutter speed, play a minor role in the optimization of experimental parameters, as they led only to slight alterations in the normalized B channels (Fig. S10). Based on these quantitative assessments, the dispersion having $C_{CDs}^{\%v/v}$ of 10 % and pH 8 was selected as the most favorable to functionalize CNPs for further pH sensing experiments.

## 3.4 pH sensing with F-CNPs: the fluorescence colorimetry approach

As demonstrated in Fig. 4 and Fig. S7, fluorescence quantification from the digital pictures can be achieved using optical emission filters to measure the intensity of either the B or the G channel, resulting in a single-channel fluorescence detection strategy. Notably, when acquiring digital pictures without emission filters (Fig. S8a-b), both the blue and green fluorescence bands are revealed simultaneously, enabling an increase in the amount of information recorded in a single acquisition. However, utilizing the sensing information from both channels simultaneously requires an image analysis strategy that cannot be only based on examining the intensity of individual B or G channels. To address this issue, the fluorescence recorded in the digital pictures is analyzed in terms of colorimetric coordinates. Fig. 5 shows the fluorescence colorimetric strategy used to sense pH with F-CNPs previously optimized (Fig. 4e-f, Fig. S8c, Table S2-S3).

The digital images in Fig. 5a depict the color of CDs fluorescence light in the absence of emission filters. Thus, the F-CNPs show a blue-green color, attributable to the combined presence

of the blue and green PL bands in the recorded light (Fig. 2d, Fig. 4). Moreover, a progressive shading from greener to bluer may be macroscopically inferred as the pH of the buffer calibration solution increases from 2.2 to 8. Although this shift can be subtle making its discernment challenging with the naked eye, it aligns with the spectroscopic trend showing an increase in the ratio between the intensity of the blue and green PL bands as pH increases (Fig. S3). To provide a more precise and objective quantification of this trend, a digital analysis of the fluorescence color was performed. Fig. 5b outlines the process for deriving colorimetric coordinates from the captured images. Similar to the method used to quantify the intensity of B and G channels reported in the SI (see Fig. S7), the digital images were analyzed to generate a data matrix.

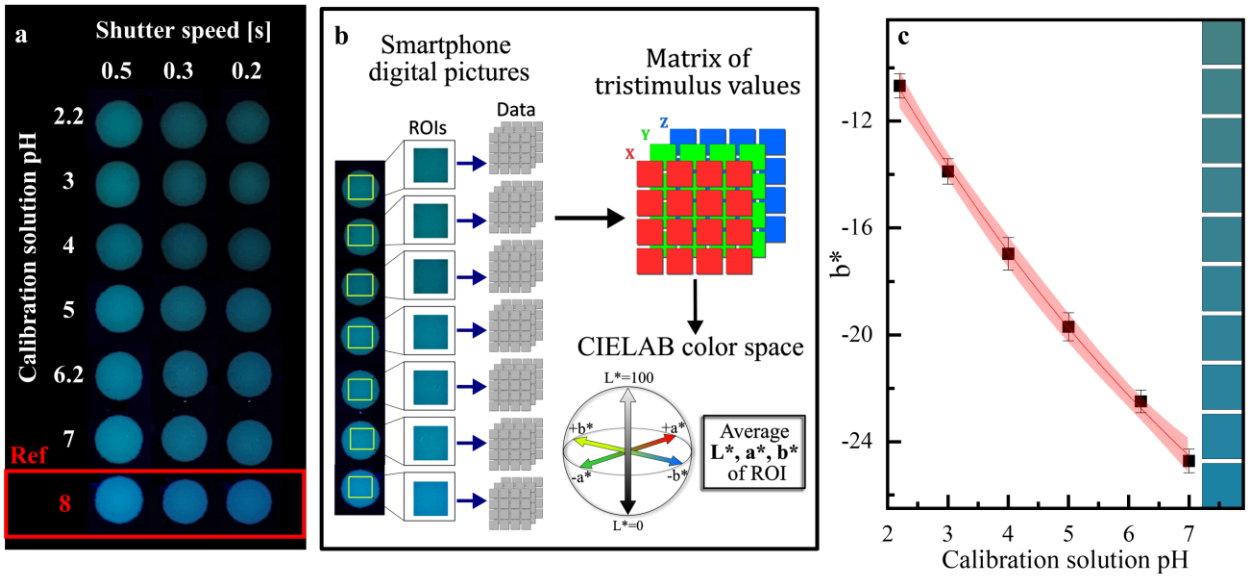


**Fig. 5.** (a) Smartphone recorded pictures obtained without emission filters at shutter speeds of 0.5, 0.3 and 0.2 s for F-CNPs functionalized with CD dispersion ML0810 (with optimized $C_{CDs}^{\%v/v}$ = 10% and pH 8, see SI) and drop-casted with buffer calibration solutions at pH of 8, 7, 6.2, 5, 4, 3, 2.2; (b) schematic description of the image analysis procedure used to obtain the CIELAB coordinates ($L^*$, $a^*$ and $b^*$) from each F-CNP; (c) $b^*$ coordinate of F-CNPs (shutter speed 0.5 s) as a function of calibration solution pH (black squares), fitted using Equation (2) (red line). The red

shaded area represents the 95% confidence interval, the error bars are standard deviations obtained from three replicates of the same experiment, the color scale legend on the right shows the perceptual colors corresponding to b* varying in the range of y-axis coordinates for fixed $L^*$ = 50 and a* = -20 (approximate average values of $L^*$ and $a^*$ obtained from the image analyses for shutter speed of 0.5 s)

This matrix contains the intensity of the R, G and B channels for each pixel in the region of interest (ROI). The R, G and B intensities were subsequently converted into X, Y and Z tristimulus values using the sRGB color space which is the native color space of the pictures. The standard illuminant assumed was D65, in line with CIE recommendations [58]. Finally, a transformation was performed to obtain CIELAB 1976 color space coordinates [59], which were averaged for each ROI. The L* variable ranges from 0 to 100 and indicates the lightness or darkness of a color, with higher values indicating lighter shades. The a* variable measures the color's position on the green-to-red axis, where negative values represent green tones and positive values represent red tones. Lastly, the b* variable indicates the color's position on the blue-to-yellow axis, with negative values indicating blue tones and positive values indicating yellow tones [58,60]. To showcase the full capabilities of our portable platform, we also successfully performed the PL colorimetric analysis directly on a smartphone using the MATLAB Mobile app, for both IOs and Android systems (Video S1). As shown in the video, the recorded image is uploaded, the F-CNPs are automatically identified, and the colorimetric evaluations are performed, yielding the average ROI coordinates as final result.

The results of the colorimetric analyses indicate that a* is affected by high experimental errors, which is consistent with its dependence from the R channel intensity, that in our case only contains noise (Fig. 4c-d). On the other hand, as shown in Fig. S11, L* is found to have the same trend with buffer calibration solution pH, as single-channel fluorescence intensity (e.g. that of B or G channels in Fig. 4e-f, or that of B channel in Fig. S8c). This is consistent with the concept that L* represents the perceptual overall lightness of the observed signal. Thus, this variable could also, in principle, be employed for pH determination through a single-channel fluorescence sensing strategy. However, as delineated in the optimization of pH sensing conditions (see SI, Fig. S8c, Table S3) the single channel methodology typically yields resolutions that do not exceed ±1 pH units. Therefore, a L*-based sensing strategy, akin to a single-channel detection method, was not applied in subsequent analyses of this work.

Nonetheless, b* is found to effectively capture the perceptual color transition observed in the pictures with changing pH. This becomes more evident when looking at the perceptual colors given by a variation of b*, when L* and a* are fixed at typical values obtained in the analyzed pictures (color scale legend in Fig. 5c). Specifically, the trend of b* as a function of calibration solution pH can be best fitted using a decreasing exponential function, of the type:

$$y = a_1 + a_2 \exp(x/a_3) \quad (3)$$

yielding $a_1 = 43 \pm 7$, $a_2 = 41 \pm 6$, $a_3 = 9 \pm 3$ and $R^2$ of 0.99877. From this fitting curve, the 95% confidence interpolation errors result of ±0.2 pH units in the pH range from 2.5 to 6.7 and of ±0.3 pH units in the pH range of 6.7 to 7.0.

This reveals an improvement compared to typical resolution allowed by the most common commercial pH indicator paper strips [5]. Recent literature works documented paper– or polymer-based colorimetric pH sensing devices that surpass the capabilities of currently available

commercial pH paper strips (i.e. ±0.5) [8–11,14–18,21,22] (Table 1). However, it is noteworthy that these studies exhibit certain limitations, including: (i) reliance on costly sensitive materials for pH detection (such as commercially available or custom-synthesized indicator dyes), (ii) complex procedures for substrate patterning (involving methods like laser patterning or customized ink-jet printing), or (iii) a restricted dynamic range spanning only 3–5 pH units [8–22,41,43,61]. In comparison, the sensing method reported herein relies on environmentally sustainable and cost-effective CDs. Moreover, it involves a user-friendly preparation approach and grants rapid pH measurement with uniform resolution across six pH units, requiring very small sample volumes.

Table 1: comparison of recently reported portable pH sensing devices based on optical detection.

| **Sensitive material** | **Support** | **Fabrication technique** | **Signal registration** | **pH range** | **pH resolution** | **Ref.** |
|---|---|---|---|---|---|---|
| Thymol blue, methyl red, bromothymol blue, phenolphthalein | Filter paper | Inkjet-printing on filter paper with hydrophilic microfluidic channels | Color scanner (Lab* color space) | 5–9 | N/A | [18] |
| Phenol red, chlorophenol red | Whatman Grade 1 filter paper | Drop-casting onto sensing areas of paper microfluidic device | Smartphone (HSV color space) | 4–9 | ±0.17 | [21] |
| Imidazole coumarin dye | Poly(methyl methacrylate)-based polymer network | Dye covalently bound to polymer by copolymerization | Fiber optic device (PL intensity) | 10.0–13.2 | < 0.5 | [17] |
| Curcumin Nanoparticles (CURN**s**) | Whatman filter paper no. 1 | Drop-casting onto hydrophilic test area of paper | Digital camera (average grayscale intensity) | 8–13 | ±0.15-0.27 | [13] |
| Indicator composed of chlorophenol red, phenol red and phenolphthalein | Whatman filter paper grade 1 | Drop-casting on detection areas of paper-based analytical device | Flatbed Scanner (magenta channel intensity) | 5–10 | ±0.2-0.4 | [61] |
| Luminol derivative (LABD) | Functionalized filter paper strips | Filter paper strips immersed in a LABD solution and left to dry | Visual | 4.0–11.0 | N/A | [10] |
| Spiropyran derivative | Cellulosic paper | Spiropyran derivative chemically attached to the paper | Visual | 1–14 | N/A | [19] |
| Rhodamine derivative (RhA) | Activated cellulose paper | RhA immobilized using a coupling agent | Visual | 1–8 | N/A | [11] |
| Two dyes based on anthraquinone and azo chromophores (D-1 and D-2) | Cellulose paper | Screen printing | Spectophotometer (Lab* color space) | 6–12 (D1)<br>1–4 (D2) | N/A | [20] |

| | | | | | | |
|---|---|---|---|---|---|---|
| pH indicators (m-nitrophenol, phenolphthalein, thymolphthalein) | Superomniphobic glass microfiber paper | pH indicators deposited in three domains created by depositing a thin layer of paraffin wax | Visual | 7.5–13 | N/A | [22] |
| SISCON pH paper | Whatman Grade 1 filter paper | pH paper attached to filter paper microfluidic channel | Smartphone camera (HSV color space) | 3–10 | N/A | [15] |
| 8 commercial pH indicators | Mixed cellulose ester (MCE) paper | Inkjet-printing on MCE paper | Color scanner (R, G, B split channel) | 1.00–13.60 | ±0.20 | [8] |
| Polyaniline nanoparticles (PAni-NPs) | Whatman quantitative filter paper (Grade 41) | Filter paper dipped in PAni-NP solution and dried, repeated 7 times | Smartphone camera (R, G, B split channels) | 2–10 | ±0.2 (pH 2-6); ±0.6 (pH 8-10) | [12] |
| Two BODIPY compounds (1a and 1b) | Whatman filter paper | Paper sheets immersed in BODIPY solutions and air-dried | Visual | 0.00–6.59 (1a) 0.00–6.28 (1b) | N/A | [9] |
| Purposely synthesized quinoxalines | Cellulose filter paper (pore size 8–12 μm) | Paper stips immersed in hot dye solution followed by drying | Visual | 1–5 | N/A | [16] |
| CDs from 1,2,4-triaminobenzene and NaOH | pH test strips | CDs incorporated in pH test strips | Visual | 1–14 | N/A | [41] |
| CDs from Aphen and citric acid | pH test paper | Inkjet printing | Visual | 1–14 | N/A | [42] |
| CDs from terephthalic acid (PTA) and o-phenylenediamine (oPD) | Poly(m-phenylene isophthalamide) (PMIA) | CDs loaded in PMIA from solution followed by casting | Smartphone camera (R, G, B split channels and CIE 1931 color space) | 1–14 | ±0.2 | [43] |
| Resorcinol-derived CDs | Nitrocellulose-based platform | Drop-casting of pristine CDs solution on nitrocellulose pads | Smartphone camera (PL analysis in Lab* color space) | 2.2–7 | ±0.2 (pH 2.5-6.7) ±0.3 (pH 6.7-7.0) | This work |

Furthermore, the present work highlights the integration of colorimetric analysis on fluorescence data acquired by portable devices to enable highly accurate sensing measurements. In fact, this is evidenced by the significantly lower resolution obtained applying a single-channel fluorescence detection (see SI, Table S3). Similar colorimetric analysis of fluorescence data obtained by portable devices was previously reported only in very few previous reports [62,63]. In this work, the fluorescence analysis approach leads to significant advance of the sensing accuracy, thanks to its capability of harnessing simultaneously the sensing information coming from the blue and the green PL bands of the CDs. Overall, given the resolution and dynamic range attainable with this

method, it appears as an effective combination of accuracy and practical operational efficacy. Therefore, the presented portable pH sensing platform is particular suited for practical applications where existing compact pH meters fail to meet necessary requirements of robustness or integrability within critical operational conditions. Similar problems could be pervasive of disparate areas, including biological samples, food chemical analyses, water quality assessment, and others [4,64–66].

## 4. Conclusions

In summary, a pH sensing platform based on nitrocellulose was developed based on the employment of CDs containing acid/base responsive PPs. First, through a comprehensive analysis of the fluorescence response of the CDs upon incremental addition of small amounts of HCl and NaOH, we established correlations between observed spectroscopic changes and the acid-base protonation-deprotonation equilibria of PPs within the CDs. This approach also enabled to devise a titration-based method, estimating an order of magnitude range for the concentration of CDs in solution. Subsequently, the CDs were used to functionalize CNPs in the nitrocellulose platform. After suitable calibrations, namely, of CD concentration, pH of pristine CD dispersion, image acquisition conditions and application of a fluorescence colorimetry image analysis (evaluating CIELAB b* coordinate), we demonstrated the achievement of a high resolution for pH reaching ±0.2 pH units in the pH range 2.5 – 6.7 and of ±0.3 pH units in the pH range: 6.7 – 7.0.

pH sensing with the resolution and dynamic range here shown could be profitable for a very broad range of applicative areas, including food, water, and biological sample analysis. In particular, this portable platform offers a solution to the challenges posed by delicate and expert-personnel requiring potentiometric pH-meters.

Looking ahead, enhancing the sensing capabilities of these platforms could be achieved through advancements in platform design and optical detection systems, as well as by optimizing

the surface chemistry of CDs, tailored for specific sample types. Such developments could pave the way for broader adoption of safe and cost-effective nanoparticles like CDs in fluorescent nitrocellulose-based portable pH sensing technologies.

## Acknowledgements

The ICN2 is funded by the CERCA programme / Generalitat de Catalunya. The ICN2 is supported by the Severo Ochoa Centres of Excellence programme, Grant CEX2021-001214-S, funded by MCIU/AEI/10.13039.501100011033. We acknowledge Departament de Recerca i Universitats of Generalitat de Catalunya for the grant 2021 SGR 01464. We also acknowledge grant PID2021-124795NB-I00 funded by MICIU/AEI/10.13039/501100011033 and by "ERDF/EU". This research was funded by the Italian MIUR PRIN 2022 SuperNano Project Prot. no. 2022C7Z2RA and by the Project ''Network 4 Energy Sustainable Transition−NEST'', code PE0000021, Concession Decree No. 1561 of 11.10.2022 of MUR (CUP B53C22004060006), financed by the European Union− NextGenerationEU under the National Recovery and Resilience Plan (NRRP), Mission 4 Component 2 Investment. M.Striccoli is grateful to the COSY Action CA21101 financed by the European Cooperation in Science and Technology (COST) programme. G. Maroli would like to express his gratitude to the Carolina Foundation for financial support through the scholarship "Doctorado 2020". G.Maroli acknowledges Universitat Autonoma de Barcelona (UAB) for the possibility of performing this work inside the framework of Chemistry PhD Programme.

# References


[1] R.P. Buck, S. Rondinini, A.K. Covington, F.G.K. Baucke, C.M.A. Brett, M.F. Camoes, M.J.T. Milton, T. Mussini, R. Naumann, K.W. Pratt, P. Spitzer, G.S. Wilson, Measurement of pH. Definition, standards, and procedures (IUPAC Recommendations 2002), Pure Appl. Chem. 74 (2002) 2169–2200. https://doi.org/10.1351/pac200274112169.

[2] H.J. Park, J.H. Yoon, K.G. Lee, B.G. Choi, Potentiometric performance of flexible pH sensor based on polyaniline nanofiber arrays, Nano Converg. 6 (2019) 9. https://doi.org/10.1186/s40580-019-0179-0.

[3] P. Spitzer, K.W. Pratt, The history and development of a rigorous metrological basis for pH measurements, J. Solid State Electrochem. 15 (2011) 69–76. https://doi.org/10.1007/s10008-010-1106-9.

[4] W. Xiao, Q. Dong, The Recent Advances in Bulk and Microfluidic-Based pH Sensing and Its Applications, Catalysts 12 (2022) 1124. https://doi.org/10.3390/catal12101124.

[5] J. Guo, L. Qiu, Z. Deng, F. Yan, Plastic reusable pH indicator strips: preparation via anion-exchange of poly(ionic liquids) with anionic dyes, Polym. Chem. 4 (2013) 1309–1312. https://doi.org/10.1039/C2PY21076B.

[6] G. Li, H. Su, N. Ma, G. Zheng, U. Kuhn, M. Li, T. Klimach, U. Pöschl, Y. Cheng, Multifactor colorimetric analysis on pH-indicator papers: an optimized approach for direct determination of ambient aerosol pH, Atmospheric Meas. Tech. 13 (2020) 6053–6065. https://doi.org/10.5194/amt-13-6053-2020.

[7] A. Collins, R.B. Scott, C.R. Hirsch, C. Ottaviani, C. Krahé, F. Meeten, A systematic review of the literature on interpretation bias and its physiological correlates, Biol. Psychol. 173 (2022).

[8] Y. Li, Y. Wang, S. Chen, Z. Wang, L. Feng, Inkjet-printed paper-based sensor array for highly accurate pH sensing, Anal. Chim. Acta 1154 (2021) 338275.

[9] D. Öztürk, İ. Ömeroğlu, B. Köksoy, C. Göl, M. Durmuş, A BODIPY decorated multiple mode reusable paper-based colorimetric and fluorometric pH sensor, Dyes Pigments 205 (2022) 110510. https://doi.org/10.1016/j.dyepig.2022.110510.

[10] Z. Yan, X. Zhang, C. Bao, H. Tang, Q. Zhao, L. Hu, J. You, A novel luminol derivative and its functionalized filter-paper for reversible double-wavelength colorimetric pH detection in fruit juice, Sens. Actuators B Chem. 262 (2018) 869–875. https://doi.org/10.1016/j.snb.2018.02.100.

[11] T. Taweetanavanich, B. Wanno, T. Tuntulani, B. Pulpoka, C. Kaewtong, A pH optical and fluorescent sensor based on rhodamine modified on activated cellulose paper, J. Chin. Chem. Soc. 66 (2019) 493–499. https://doi.org/10.1002/jccs.201800327.

[12] T. Lee, H.-T. Lee, J. Hong, S. Roh, D. Yeon Cheong, K. Lee, Y. Choi, Y. Hong, H.-J. Hwang, G. Lee, A regression-based machine learning approach for pH and glucose detection with redox-sensitive colorimetric paper sensors, Anal. Methods 14 (2022) 4749–4755. https://doi.org/10.1039/D2AY01329K.

[13] N. Pourreza, H. Golmohammadi, Application of curcumin nanoparticles in a lab-on-paper device as a simple and green pH probe, Talanta 131 (2015) 136–141. https://doi.org/10.1016/j.talanta.2014.07.063.

[14] J. Ling, G. Naren, J. Kelly, T.S. Moody, A.P. de Silva, Building pH Sensors into Paper-Based Small-Molecular Logic Systems for Very Simple Detection of Edges of Objects, J. Am. Chem. Soc. 137 (2015) 3763–3766. https://doi.org/10.1021/jacs.5b00665.

[15] O.R. Chanu, A. Kapoor, V. Karthik, Digital image analysis for microfluidic paper based pH sensor platform, Mater. Today Proc. 40 (2021) S64–S68. https://doi.org/10.1016/j.matpr.2020.03.503.
[16] E.V. Ermakova, A.V. Bol'shakova, A. Bessmertnykh-Lemeune, Dual-Responsive and Reusable Optical Sensors Based on 2,3-Diaminoquinoxalines for Acidity Measurements in Low-pH Aqueous Solutions, Sensors 23 (2023) 2978. https://doi.org/10.3390/s23062978.
[17] T.H. Nguyen, T. Venugopala, S. Chen, T. Sun, K.T.V. Grattan, S.E. Taylor, P.A.M. Basheer, A.E. Long, Fluorescence based fibre optic pH sensor for the pH 10–13 range suitable for corrosion monitoring in concrete structures, Sens. Actuators B Chem. 191 (2014) 498–507. https://doi.org/10.1016/j.snb.2013.09.072.
[18] K. Abe, K. Suzuki, D. Citterio, Inkjet-Printed Microfluidic Multianalyte Chemical Sensing Paper, Anal. Chem. 80 (2008) 6928–6934. https://doi.org/10.1021/ac800604v.
[19] A. Abdollahi, A. Mouraki, M.H. Sharifian, A.R. Mahdavian, Photochromic properties of stimuli-responsive cellulosic papers modified by spiropyran-acrylic copolymer in reusable pH-sensors, Carbohydr. Polym. 200 (2018) 583–594. https://doi.org/10.1016/j.carbpol.2018.08.042.
[20] H. Zhang, A. Hou, K. Xie, A. Gao, Smart color-changing paper packaging sensors with pH sensitive chromophores based on azo-anthraquinone reactive dyes, Sens. Actuators B Chem. 286 (2019) 362–369. https://doi.org/10.1016/j.snb.2019.01.165.
[21] N. Lopez-Ruiz, V.F. Curto, M.M. Erenas, F. Benito-Lopez, D. Diamond, A.J. Palma, L.F. Capitan-Vallvey, Smartphone-Based Simultaneous pH and Nitrite Colorimetric Determination for Paper Microfluidic Devices, Anal. Chem. 86 (2014) 9554–9562. https://doi.org/10.1021/ac5019205.
[22] S. Movafaghi, M.D. Cackovic, W. Wang, H. Vahabi, A. Pendurthi, C.S. Henry, A.K. Kota, Superomniphobic Papers for On-Paper pH Sensors, Adv. Mater. Interfaces 6 (2019) 1900232. https://doi.org/10.1002/admi.201900232.
[23] H. LEE, M.R. HAM, H. KIM, S. KIM, Hydrogel coating composition for chemical sensor and chemical sensor fabricated using same, WO2022030754A1, 2022.
[24] Y.S. KIM, Y.-B. CHO, T.-S. JUN, C.K. KIM, Paper ph sensor using colorimetric method and preparation method thereof, WO2016159488A1, 2016.
[25] K. Perez, L. NELSON, T. Robinson, A. FREANEY, H. VAN, A. OLANREWAJU, G.C. VALENTINE, E.J. Seibel, E. Fan, J.D. POSNER, M. SHARMA, Sensor paper and methods for use, WO2023086993A1, 2023.
[26] H. Ehtesabi, Z. Hallaji, S. Najafi Nobar, Z. Bagheri, Carbon dots with pH-responsive fluorescence: a review on synthesis and cell biological applications, Microchim. Acta 187 (2020) 150. https://doi.org/10.1007/s00604-019-4091-4.
[27] V.M. Naik, S.V. Bhosale, G.B. Kolekar, A brief review on the synthesis, characterisation and analytical applications of nitrogen doped carbon dots, Anal. Methods 14 (2022) 877–891. https://doi.org/10.1039/D1AY02105B.
[28] A.O. Adeola, A. Clermont-Paquette, A. Piekny, R. Naccache, Advances in the design and use of carbon dots for analytical and biomedical applications, Nanotechnology 35 (2023) 012001. https://doi.org/10.1088/1361-6528/acfdaf.
[29] S. Chahal, J.-R. Macairan, N. Yousefi, N. Tufenkji, R. Naccache, Green synthesis of carbon dots and their applications, RSC Adv. 11 (2021) 25354–25363. https://doi.org/10.1039/D1RA04718C.

[30] J. Wan, X. Zhang, Y. Jiang, S. Xu, J. Li, M. Yu, K. Zhang, Z. Su, Regulation of multi-color fluorescence of carbonized polymer dots by multiple contributions of effective conjugate size, surface state, and molecular fluorescence, J. Mater. Chem. B 10 (2022) 6991–7002. https://doi.org/10.1039/D2TB01330D.
[31] B. Han, X. Hu, X. Zhang, X. Huang, M. An, X. Chen, D. Zhao, J. Li, The fluorescence mechanism of carbon dots based on the separation and identification of small molecular fluorophores, RSC Adv. 12 (2022) 11640–11648. https://doi.org/10.1039/D2RA00431C.
[32] A. Sharma, J. Das, Small molecules derived carbon dots: synthesis and applications in sensing, catalysis, imaging, and biomedicine, J. Nanobiotechnology 17 (2019) 92. https://doi.org/10.1186/s12951-019-0525-8.
[33] A. Sharma, T. Gadly, S. Neogy, S.K. Ghosh, M. Kumbhakar, Molecular Origin and Self-Assembly of Fluorescent Carbon Nanodots in Polar Solvents, J. Phys. Chem. Lett. 8 (2017) 1044–1052. https://doi.org/10.1021/acs.jpclett.7b00170.
[34] S. Qu, H. Chen, X. Zheng, J. Cao, X. Liu, Ratiometric fluorescent nanosensor based on water soluble carbon nanodots with multiple sensing capacities, Nanoscale 5 (2013) 5514–5518. https://doi.org/10.1039/C3NR00619K.
[35] Q. Zhao, Y. Li, W. Wei, J. Huang, D. Lu, S. Liu, X. Shi, A ratiometric fluorescence-based colorimetric sensor for the portable analysis of antioxidants via smartphone, Microchem. J. 190 (2023) 108625. https://doi.org/10.1016/j.microc.2023.108625.
[36] H. Nie, M. Li, Q. Li, S. Liang, Y. Tan, L. Sheng, W. Shi, S.X.-A. Zhang, Carbon Dots with Continuously Tunable Full-Color Emission and Their Application in Ratiometric pH Sensing, Chem. Mater. 26 (2014) 3104–3112. https://doi.org/10.1021/cm5003669.
[37] J. Zhang, H. Chen, K. Xu, D. Deng, Q. Zhang, L. Luo, Current Progress of Ratiometric Fluorescence Sensors Based on Carbon Dots in Foodborne Contaminant Detection, Biosensors 13 (2023) 233. https://doi.org/10.3390/bios13020233.
[38] W.K. Szapoczka, C. Olla, C. Carucci, A.L. Truskewycz, T. Skodvin, A. Salis, C.M. Carbonaro, B. Holst, P.J. Thomas, Ratiometric Fluorescent pH Sensing with Carbon Dots: Fluorescence Mapping across pH Levels for Potential Underwater Applications, Nanomaterials 14 (2024) 1434. https://doi.org/10.3390/nano14171434.
[39] A. Heering, M. Lahe, M. Vilbaste, J. Saame, J. Paulo Samin, I. Leito, Improved pH measurement of mobile phases in reversed-phase liquid chromatography, Analyst (2024). https://doi.org/10.1039/D3AN02029K.
[40] L. Deleebeeck, A. Snedden, D. Nagy, Z. Szilágyi Nagyné, M. Roziková, M. Vičarová, A. Heering, F. Bastkowski, I. Leito, R. Quendera, V. Cabral, D. Stoica, Unified pH Measurements of Ethanol, Methanol, and Acetonitrile, and Their Mixtures with Water, Sensors 21 (2021) 3935. https://doi.org/10.3390/s21113935.
[41] L. Wang, M. Li, W. Li, Y. Han, Y. Liu, Z. Li, B. Zhang, D. Pan, Rationally Designed Efficient Dual-Mode Colorimetric/Fluorescence Sensor Based on Carbon Dots for Detection of pH and Cu2+ Ions, ACS Sustain. Chem. Eng. 6 (2018) 12668–12674. https://doi.org/10.1021/acssuschemeng.8b01625.
[42] T. Zhang, S. Dong, F. Zhao, M. Deng, Y. Fu, C. Lü, Tricolor emissive carbon dots for ultra-wide range pH test papers and bioimaging, Sens. Actuators B Chem. 298 (2019) 126869. https://doi.org/10.1016/j.snb.2019.126869.
[43] K. Huo, J. Zhang, T. Lin, Y. Zhang, Y. Liu, X. Liu, Colorimetric and fluorescent dual-mode pH sensor with PMIA as substrate and CQDs as probe for high accuracy detection of

full range pH, Dyes Pigments 219 (2023) 111574. https://doi.org/10.1016/j.dyepig.2023.111574.
[44] G. Minervini, A. Panniello, A. Madonia, C.M. Carbonaro, F. Mocci, T. Sibillano, C. Giannini, R. Comparelli, C. Ingrosso, N. Depalo, E. Fanizza, M.L. Curri, M. Striccoli, Photostable carbon dots with intense green emission in an open reactor synthesis, Carbon 198 (2022) 230–243. https://doi.org/10.1016/j.carbon.2022.07.034.
[45] T.C. McIlvaine, A BUFFER SOLUTION FOR COLORIMETRIC COMPARISON, J. Biol. Chem. 49 (1921) 183–186. https://doi.org/10.1016/S0021-9258(18)86000-8.
[46] G. Knobel, On The Capillary Electrophoresis Of Monohydroxy Metabolites Of Polycyclic Aromatic Hydrocarbons And Its Application To The Analysis Of Biological Matrices, Electron. Theses Diss. (2013). https://stars.library.ucf.edu/etd/2858.
[47] H. Rastogi, S. Jana, Evaluation of physicochemical properties and intestinal permeability of six dietary polyphenols in human intestinal colon adenocarcinoma Caco-2 cells, Eur. J. Drug Metab. Pharmacokinet. 41 (2016) 33–43. https://doi.org/10.1007/s13318-014-0234-5.
[48] T. Mao, F.N.U. Akshit, I. Matiwalage, S. Sasidharan, C.M. Alvarez, P. Wescombe, M.S. Mohan, Preferential Binding of Polyphenols in Blackcurrant Extracts with Milk Proteins and the Effects on the Bioaccessibility and Antioxidant Activity of Polyphenols, Foods 13 (2024) 515. https://doi.org/10.3390/foods13040515.
[49] J. Shang, X. Gao, Nanoparticle counting: towards accurate determination of the molar concentration, Chem Soc Rev 43 (2014) 7267–7278. https://doi.org/10.1039/C4CS00128A.
[50] W. Bae, T.-Y. Yoon, C. Jeong, Direct evaluation of self-quenching behavior of fluorophores at high concentrations using an evanescent field, PLOS ONE 16 (2021) e0247326. https://doi.org/10.1371/journal.pone.0247326.
[51] J. Wachlmayr, C. Hannesschlaeger, A. Speletz, T. Barta, A. Eckerstorfer, C. Siligan, A. Horner, Scattering versus fluorescence self-quenching: more than a question of faith for the quantification of water flux in large unilamellar vesicles?, Nanoscale Adv. 4 (2022) 58–76. https://doi.org/10.1039/D1NA00577D.
[52] W.F. Watson, R. Livingston, Self-Quenching and Sensitization of Fluorescence of Chlorophyll Solutions, J. Chem. Phys. 18 (2004) 802–809. https://doi.org/10.1063/1.1747779.
[53] Y. Song, S. Zhu, S. Xiang, X. Zhao, J. Zhang, H. Zhang, Y. Fu, B. Yang, Investigation into the fluorescence quenching behaviors and applications of carbon dots, Nanoscale 6 (2014) 4676–4682. https://doi.org/10.1039/C4NR00029C.
[54] J. Wang, Y. Yang, X. Liu, Solid-state fluorescent carbon dots: quenching resistance strategies, high quantum efficiency control, multicolor tuning, and applications, Mater. Adv. 1 (2020) 3122–3142. https://doi.org/10.1039/D0MA00632G.
[55] F. Zu, F. Yan, Z. Bai, J. Xu, Y. Wang, Y. Huang, X. Zhou, The quenching of the fluorescence of carbon dots: A review on mechanisms and applications, Microchim. Acta 184 (2017) 1899–1914. https://doi.org/10.1007/s00604-017-2318-9.
[56] C. Wei, S. Hu, F. Liang, Z. Song, X. Liu, One-pot synthesis of concentration and excitation dual-dependency truly full-color photoluminescence carbon dots, Chin. Chem. Lett. 33 (2022) 4116–4120. https://doi.org/10.1016/j.cclet.2022.01.053.
[57] C.J. Reckmeier, J. Schneider, Y. Xiong, J. Häusler, P. Kasák, W. Schnick, A.L. Rogach, Aggregated Molecular Fluorophores in the Ammonothermal Synthesis of Carbon Dots, Chem. Mater. 29 (2017) 10352–10361. https://doi.org/10.1021/acs.chemmater.7b03344.

[58] J. Schanda, International Commission on Illumination, eds., Colorimetry: understanding the CIE system, CIE/Commission internationale de l'eclairage ; Wiley-Interscience, [Vienna, Austria] : Hoboken, N.J, 2007.
[59] J. Schanda, CIE u′, v′ Uniform Chromaticity Scale Diagram and CIELUV Color Space, in: M.R. Luo (Ed.), Encycl. Color Sci. Technol., Springer, New York, NY, 2016: pp. 185–188. https://doi.org/10.1007/978-1-4419-8071-7_12.
[60] C. Oleari, Standard colorimetry: definitions, algorithms, and software, John Wiley & Sons, Inc, Chichester, West Sussex, UK, 2016.
[61] J. Noiphung, M.P. Nguyen, C. Punyadeera, Y. Wan, W. Laiwattanapaisal, C.S. Henry, Development of Paper-Based Analytical Devices for Minimizing the Viscosity Effect in Human Saliva, Theranostics 8 (2018) 3797–3807. https://doi.org/10.7150/thno.24941.
[62] J. Yang, Z. Li, Q. Jia, Design of dual-emission fluorescence sensor based on Cu nanoclusters with solvent-dependent effects: Visual detection of water via a smartphone, Sens. Actuators B Chem. 297 (2019) 126807. https://doi.org/10.1016/j.snb.2019.126807.
[63] Spatially confining copper nanoclusters in porous ZrO2 for fluorescence/colorimetry/smartphone triple-mode detection of metoprolol tartrate, Biosens. Bioelectron. 231 (2023) 115290. https://doi.org/10.1016/j.bios.2023.115290.
[64] L. Manjakkal, S. Dervin, R. Dahiya, Flexible potentiometric pH sensors for wearable systems, RSC Adv. 10 (2020) 8594–8617. https://doi.org/10.1039/D0RA00016G.
[65] M.T. Ghoneim, A. Nguyen, N. Dereje, J. Huang, G.C. Moore, P.J. Murzynowski, C. Dagdeviren, Recent Progress in Electrochemical pH-Sensing Materials and Configurations for Biomedical Applications, Chem. Rev. (2019). https://doi.org/10.1021/acs.chemrev.8b00655.
[66] Y. Tang, L. Zhong, W. Wang, Y. He, T. Han, L. Xu, X. Mo, Z. Liu, Y. Ma, Y. Bao, S. Gan, L. Niu, Recent Advances in Wearable Potentiometric pH Sensors, Membranes 12 (2022) 504. https://doi.org/10.3390/membranes12050504.